JOURNAL OF COMPUTATIONAL PHYSICS **126,** 21–39 (1996)
ARTICLE NO. 0117

Numerical Study of a Three-Dimensional Chemical Vapor Deposition Reactor with Detailed Chemistry

ALEXANDRE ERN,*,†,‡ VINCENT GIOVANGIGLI,† AND MITCHELL D. SMOOKE‡

*CERMICS-ENPC, 93167 Noisy-le-Grand cedex, France; †CMAP-CNRS, Ecole Polytechnique, 91128 Palaiseau cedex, France; and ‡Department of Mechanical Engineering, Yale University, P.O. Box 208284, New Haven, Connecticut 06520-8284

Received May 9, 1995; revised November 10, 1995

A numerical model of a three-dimensional, horizontal channel, chemical vapor deposition reactor is presented in order to study gallium arsenide growth from trimethylgallium and arsine source reactants. Fluid flow and temperature predictions inside the reactor are obtained using the vorticity-velocity form of the three-dimensional, steady-state Navier–Stokes equations coupled with a detailed energy balance equation inside the reactor and on its walls. Detailed gas phase and surface chemistry mechanisms are used to predict the chemical species profiles inside the reactor, the growth rate distribution on the substrate, and the level of carbon incorporation into the grown layer. The species diffusion velocities are written using the recent theory of iterative transport algorithms and account for both thermal diffusion and multicomponent diffusion processes. The influence of susceptor temperature and inlet composition on growth rate and carbon incorporation is found to agree well with previous numerical and experimental work.

1. INTRODUCTION

Chemical vapor deposition (CVD) has established itself as an industrially important technique for manufacturing thin solid films to be used in optoelectronic devices and high speed digital circuits. The success of this technique primarily stems from its flexibility, its relative simplicity, and the high compositional control it offers. A system of particular interest is the growth of III–V compound epitaxial layers from metalorganic and hydride compounds [1, 2]. Although CVD reactors are often used for commercial throughput, efficient equipment design, and device property improvement still require further understanding of the various physical and chemical processes involved. In this context, the development of accurate numerical models is particularly attractive in order to study the influence of various operating parameters on product quality.

The CVD process involves introducing metered amounts of gaseous compounds into a reactor that contains a substrate placed on a heated susceptor, as shown in Fig. 1. A detailed picture of the chemical reactor must, therefore, account for several important effects, including description of the flow field and the temperature distribution inside the reactor, chemical reactions in the gas phase and on the substrate surface, and multicomponent diffusion processes of precursor species in the gas phase due to temperature and concentration gradients. As a result, most of the numerical models derived in the past have invoked simplifying assumptions, thereby focusing either on multidimensional flow field and temperature predictions or on chemistry aspects.

In the first approach, priority is given to understanding heat and mass transfer inside the CVD reactor while the growth rate is estimated in some simple form, e.g., by assuming that the deposition process is diffusion limited. With the significant increase in computer capabilities over the last decade, CVD flow models have expanded from two-dimensional simulations [3–11] and parabolic three-dimensional models [12, 13] to full three-dimensional calculations [14–16]. A better understanding of mixed convection flows has emerged from these studies, including the influence of various operating parameters on transverse motion and return flows above the leading edge of the susceptor. Furthermore, the pioneering work of Moffat and Jensen [12, 13] has revealed the importance of temperature boundary conditions in order to obtain accurate fluid flow and temperature predictions for several reactor configurations. As a result, most of the recently derived CVD numerical models have accounted for detailed energy balance at the reactor walls, including internal radiation from the susceptor, external radiation to the surrounding region, heat conduction in the walls and from the hot gases inside the reactor, and natural or forced heat transfer [9, 10].

While fluid flow phenomena and overall growth behavior provide useful insight into the origin of layer thickness variations, the incorporation of gas phase and surface chemical kinetics into the model is essential for a more detailed and complete understanding of the CVD process. Numerical simulations with detailed chemical reaction schemes have first appeared for ideal flow geometries, including impinging jets, boundary layer two-dimensional models, and rotating disks [17–20]. Fully elliptic simula-

0021-9991/96 $18.00

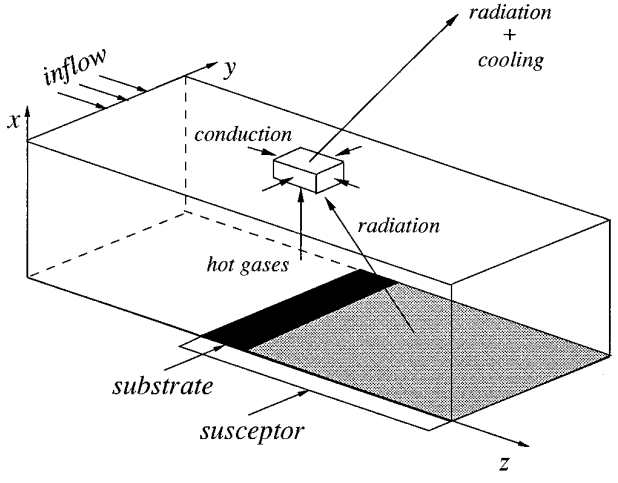

FIG. 1. Schematic of the three-dimensional CVD reactor with an elementary wall element illustrating the detailed heat transfer balance.

tions with detailed gas phase and one-step surface chemistry have been presented in two [21] and three dimensions [22]. Recent advances in the understanding of gas phase and especially surface kinetics of metalorganic CVD systems have significantly expanded modeling capabilities by giving deeper insight into the growth process and the mechanism leading to carbon incorporation into the epitaxial layer [16, 23, 24].

The goal of the present work is now to derive a numerical model of a three-dimensional, horizontal channel, metalorganic CVD reactor which predicts the flow patterns and the temperature distribution inside the reactor and also accounts for detailed chemistry processes both in the gas phase and on the surface. The present model incorporates for the first time a detailed and accurate model for multicomponent diffusion of precursor species in the gas phase. Indeed, the species diffusion velocities due to concentration and temperature gradients are evaluated using the recent theory of multicomponent transport algorithms [25]. The chemical process considered is the growth of gallium arsenide (GaAs) using trimethyl-gallium ($Ga(CH_3)_3$) and arsine (AsH_3) source compounds. The model predictions are compared against previous numerical and experimental work. With the wide variety of reactor configurations reported in the literature, the aim of the present model is to reproduce trends in growth and carbon incorporation predictions rather than fitting parameters to match a given set of data. A sensitivity analysis is also included in order to emphasize the critical reaction steps in the surface chemistry mechanism. The paper is organized as follows. In the next section we derive the physical model of the CVD reactor. In Section 3, we next describe the numerical solution method. Finally, numerical results are presented in Section 4.

2. DERIVATION OF THE PHYSICAL MODEL

2.1. *Governing Equations*

The governing equations for the CVD reactor model express the conservation of total mass, momentum, energy, and gas phase species mass. The specification of the governing equations is then completed with boundary conditions accounting, in particular, for heat transfer at the reactor walls and surface chemistry processes on the substrate. Despite the high level of complexity of the physical and chemical phenomena involved, some simplifying assumptions can still be invoked in order to cast the model in a more efficient form to be analyzed numerically.

First, the epitaxial layer growth rate is typically of the order of a fraction of a micrometer per minute. As a consequence, the conservation equations are written in steady-state form and the geometry of the reactor is kept constant with time. Second, typical operating conditions for CVD reactors lead to low speed, laminar flows and the kinetic energy contribution in the energy equation can be neglected. Finally, the heat release due to chemical reactions and the enthalpy flux are negligible in the energy balance [23]. As a result, the basic conservation equations for the CVD reactor may be written as

Total mass,

$$\nabla \cdot (\rho v) = 0; \tag{1}$$

Momentum,

$$\nabla \cdot (\rho v \otimes v) = -\nabla \cdot \Pi + \rho g; \tag{2}$$

Energy,

$$\nabla \cdot (\rho v h) = -\nabla \cdot (\lambda \nabla T); \tag{3}$$

Species mass,

$$\nabla \cdot (\rho v Y_i) = -\nabla \cdot (\rho Y_i V_i) + W_i \omega_i, \quad i = 1, ..., n^{(g)}. \tag{4}$$

Here, ∇ denotes the three-dimensional space derivative operator, ρ the density, v the mass averaged flow velocity, $v \otimes v$ the velocity tensor of rank two, Π the pressure tensor, and $\nabla \cdot \Pi$ its divergence, g the gravitational acceleration, h the specific enthalpy of the mixture, λ the thermal conductivity, T the temperature, Y_i the mass fraction of the ith species, V_i its diffusion velocity, W_i its molecular weight, ω_i its molar production rate, and $n^{(g)}$ the number of gas phase species. In addition, the

pressure tensor Π and the species diffusion velocities V_i may be expressed as

$$\Pi = pI - \left(\kappa - \frac{2}{3}\eta\right)(\nabla \cdot v)I - \eta(\nabla v + (\nabla v)^t), \quad (5)$$

$$V_i = -\sum_{j=1}^{n^{(g)}} D_{ij}\nabla X_j - \theta_i \nabla \log T, \quad i = 1, ..., n^{(g)}, \quad (6)$$

where p is the pressure, I the identity matrix, κ the volume viscosity, η the shear viscosity, D_{ij}, $1 \le i, j \le n^{(g)}$, the species diffusion coefficients, X_i the mole fraction of the ith species, and θ_i, $1 \le i \le n^{(g)}$, the thermal diffusion coefficients. Finally, using the ideal gas law, the density is expressed as

$$\rho = pW/RT, \quad (7)$$

where $W = \sum_{i=1}^{n^{(g)}} X_i W_i$ is the mean molecular weight of the mixture and R is the gas constant.

Under typical operating conditions, the reactants are diluted in a carrier gas. Therefore, we may assume that the physical properties of the gas mixture are independent of the variations in mixture composition due to chemical reactions. The density is formed using a mean molecular weight based on the carrier gas and arsine at inflow concentrations [5, 15]. Because of the large V/III element ratio used in CVD reactors, the depletion of arsine through the reactor has a negligible effect on the density. On the other hand, the shear viscosity, the thermal conductivity, and the specific enthalpy can be taken to match those of the carrier gas. These quantities are recovered as a function of temperature from a thermodynamical data base [26]. With these assumptions, a two-step procedure can be used to solve the governing equations (1)–(4). Equations (1)–(3) form the ''flow problem'' and are solved coupled together in a first step. Their solution provides the fluid flow and temperature distribution inside the CVD reactor. In a second step, the ''chemistry problem'' consisting of the $n^{(g)}$ species conservation equations (4) is solved using the velocity and temperature profiles resulting from the flow problem. The flow problem and the chemistry problem are discussed in the following two sections.

2.2. *The Vorticity-Velocity Formulation for the Flow Problem*

The total mass and momentum conservation equations (1)–(2) are written in the previous section in primitive variable form, i.e., in terms of the velocity vector $v = (v_i)_{i\in[1,3]}$ and the pressure p. The major numerical difficulty associated with the primitive variable formulation is the ability to obtain a smooth pressure field in a form consistent with the discrete continuity equation. When using finite differences, the most common way to overcome this difficulty is to use a staggered grid arrangement. However, staggered mesh schemes meet with difficulties when using locally adapted grids, multigrid methods, or generalized curvilinear coordinates [27, 28]. The use of body-fitted generalized curvilinear coordinates is particularly relevant to CVD reactor modeling since reactors often have a complex geometry and may include a tilted susceptor in order to achieve higher spatial uniformity of the epitaxial layer. Although tilted susceptors are not considered in the present model, we intend to include them in future work and, as such, we prefer not to use a staggered grid in this study.

While the stream function-vorticity formulation is relatively cumbersome in three dimensions, the Navier–Stokes equations can be conveniently written in vorticity-velocity form. This formulation uses the three-dimensional vorticity vector $\zeta = (\zeta_i)_{i\in[1,3]}$ which is the curl of the velocity, i.e.,

$$\zeta = \nabla \times v. \quad (8)$$

Various numerical simulations of low to moderate Reynolds number incompressible flows have been reported using the vorticity-velocity formulation (see [29] for a review). This formulation is particularly suited to steady state, low speed, compressible flows [22, 30]. It has been successfully applied to simulate mixed convection problems in ducts and cavities [30, 31] and, more recently, to study multidimensional laminar flames with detailed chemistry [32]. Thus, CVD reactor models constitute an industrially important class of problems that can be efficiently handled using this formulation. The main advantage of the vorticity-velocity formulation is that it casts the governing equations in a fully elliptic form, thus yielding a stable and cost-effective solution algorithm. In addition, the governing equations can be discretized on a single grid.

The derivation of the vorticity-velocity formulation for three-dimensional compressible flows is given in [22, 30] so that only the basic equations are restated here. The vorticity transport equation is formed by taking the curl of the momentum conservation equation (2). After some algebra, we obtain

$$\begin{aligned}\nabla \times (\zeta \times (\rho v)) + \nabla\rho \times \nabla \frac{v^2}{2} = \nabla\rho \times g + \eta \nabla^2 \zeta \\ + D^{(1)}(\eta) + D^{(2)}(\eta),\end{aligned} \quad (9)$$

where the three-dimensional vectors $D^{(1)}(\eta)$ and $D^{(2)}(\eta)$ contain, respectively, all the first- and second-order derivatives of the viscosity and are given by

$$\begin{aligned}D^{(1)}(\eta) &= -\nabla\eta \times (\nabla \times \zeta - 2\nabla(\nabla \cdot v)) + \nabla\zeta \cdot \nabla\eta, \\ D_i^{(2)}(\eta) &= \sum_{j,k,l\in[1,3]} \varepsilon_{ijk}\partial_{jl}^2 \eta(\partial_l v_k + \partial_k v_l), \quad i \in [1,3].\end{aligned} \quad (10)$$

Here, ∂_k denotes spatial differentiation in the kth spatial coordinate and $\varepsilon_{ijk} = 1$ if (ijk) is an even permutation of (123), $\varepsilon_{ijk} = -1$ if (ijk) is an odd permutation of (123), and $\varepsilon_{ijk} = 0$ otherwise. On the other hand, an elliptic, Laplace type equation is derived for each of the three velocity components by taking the curl of (8) and using the continuity equation (1), yielding

$$\nabla^2 v = -\nabla \times \zeta - \nabla \left(\frac{v \cdot \nabla \rho}{\rho} \right). \tag{11}$$

The vorticity-velocity form of the flow problem thus consists of Eqs. (3), (9), and (11). These equations form a coupled system of partial differential equations for the dependent variables which are the velocity vector, the vorticity vector, and the temperature. Note that the increase of dependent variables with respect to the primitive variable formulation is not critical for the present problem since the most demanding step for computer resources is the solution of the chemistry problem. On the other hand, the continuity equation is obtained as a result of the computation, as discussed in [22].

To complete the specification of the governing equations in vorticity-velocity form, boundary conditions must be applied to all sides of the domain illustrated in Fig. 1. Since the flow is symmetric in the y direction (the transverse direction), the computational domain consists of only half of the reactor shown in Fig. 1. At the inflow plane, the temperature and the velocity profiles are specified and the vorticity is evaluated from its definition (8) using a second-order scheme [32]. The velocity profile corresponds to a fully developed flow in a rectangular duct as given in [33]. At the outflow boundary, all the normal derivatives of the dependent variables are assumed to vanish, thus simulating fully developed conditions. On solid walls, the velocity vector is set to zero and the vorticity is again recovered from its definition (8) using a second-order scheme [32]. The susceptor temperature is held constant while on the remaining walls the temperature is obtained through a detailed energy balance. The energy flux to a wall element is composed of four contributions: radiant heat transfer from the susceptor and to the surroundings, cooling by the surrounding gas, heat conduction from the reactor gases, and heat conduction inside the quartz wall [10]. The explicit form of the temperature boundary condition is detailed in Appendix A.

2.3. *Detailed Chemistry Model*

The solution of the conservation equations (1)–(3) using the vorticity-velocity formulation provides profiles for the velocity vector v and the temperature T inside the reactor and on its boundaries. These profiles are subsequently used to solve the species mass conservation equations (4). In the present model, the conservation equations (4) are solved for all the gas phase species except for the carrier gas. The mass fraction of the carrier gas is recovered from the mass conservation constraint $\sum_{i=1}^{n^{(g)}} Y_i = 1$. In this paper we assume, without loss of generality, that the carrier gas is ordered as the last species.

The specification of the species diffusion velocities (6) requires the evaluation of various transport properties, i.e., the species diffusion coefficients and the thermal diffusion coefficients. The transport properties are evaluated using the recent theory of multicomponent transport algorithms [25]. This theory provides accurate and computationally effective approximations for all the transport coefficients of gas mixtures. For a detailed discussion of the cost-effectiveness of these algorithms in multicomponent flow simulations, we refer to [34]. It is also worthwhile to note that in the framework of this theory, the species diffusion coefficients are symmetric, $D_{ij} = D_{ji}$ for $1 \le i, j \le n^{(g)}$, and they also yield a positive entropy production on the hyperplane of zero-sum gradients. Furthermore, the diffusion velocities automatically satisfy the mass conservation constraint

$$\sum_{i=1}^{n^{(g)}} Y_i V_i = 0. \tag{12}$$

The explicit expression for the thermal diffusion coefficients is lengthy and is omitted for brevity [25, 35]. On the other hand, for compact notation, we introduce the flux diffusion matrix $\tilde{D} = (\tilde{D}_{ij})_{1 \le i,j \le n^{(g)}}$ with $\tilde{D}_{ij} = Y_i D_{ij}$ [36]. The flux diffusion matrix may then be written as [35]

$$\tilde{D} = P \, \Delta P, \tag{13}$$

where P is the projector matrix given by $P_{ij} = \delta_{ij} - Y_i$, $1 \le i, j \le n^{(g)}$, and δ_{ij} is the Kronecker symbol. In addition, the matrix Δ may be expressed as

$$\begin{aligned} \Delta_{ii} &= \frac{W_i}{W} d_i (1 + Y_i), \qquad 1 \le i \le n^{(g)}, \\ \Delta_{ij} &= \frac{W_i}{W} d_i d_j \frac{X_i}{\mathscr{D}_{ij}}, \qquad 1 \le i, j \le n^{(g)}, \, i \ne j. \end{aligned} \tag{14}$$

Here, the quantity d_i is given by

$$d_i = (1 - Y_i) \left(\sum_{\substack{j=1 \\ j \ne i}}^{n^{(g)}} \frac{X_j}{\mathscr{D}_{ij}} \right)^{-1}, \quad 1 \le i \le n^{(g)}, \tag{15}$$

where $\mathscr{D}_{ij}$ is the binary diffusion coefficient for species pair (i, j). A simplification that is often invoked for the diffusion matrix is the use of the dilution limit, i.e., the diffusion

TABLE I

Gas Phase Reaction Mechanism

Reaction	A	β	E
G1. $Ga(CH_3)_3 \rightleftharpoons Ga(CH_3)_2 + CH_3$	3.5E + 15	0.0	59500.
G2. $Ga(CH_3)_2 \rightleftharpoons GaCH_3 + CH_3$	8.7E + 07	0.0	35400.
G3. $Ga(CH_3)_3 + H \rightleftharpoons Ga(CH_3)_2 + CH_4$	5.0E + 13	0.0	10000.
G4. $Ga(CH_3)_2 + H \rightleftharpoons GaCH_3 + CH_4$	5.0E + 13	0.0	10000.
G5. $Ga(CH_3)_3 + CH_3 \rightleftharpoons Ga(CH_3)_2CH_2 + CH_4$	2.0E + 11	0.0	10000.
G6. $Ga(CH_3)_2CH + H \rightleftharpoons Ga(CH_3)_3$	1.0E + 14	0.0	0.
G7. $Ga(CH_3)_2 + CH_3 \rightleftharpoons Ga(CH_3)CH_2 + CH_4$	2.0E + 11	0.0	10000.
G8. $Ga(CH_3)CH_2 + H \rightleftharpoons Ga(CH_3)_2$	1.0E + 14	0.0	0.
G9. $Ga(CH_3) + CH_3 \rightleftharpoons Ga(CH_2) + CH_4$	2.0E + 11	0.0	10000.
G10. $Ga(CH_2) + H \rightleftharpoons Ga(CH_3)$	1.0E + 14	0.0	0.
G11. $Ga(CH_3)_2CH_2 \rightleftharpoons Ga(CH_3)CH_2 + CH_3$	3.5E + 15	0.0	59500.
G12. $Ga(CH_3)CH_2 \rightleftharpoons GaCH_2 + CH_3$	8.7E + 07	0.0	35400.
G13. $H + H + M \rightleftharpoons H_2 + M$	1.0E + 16	0.0	0.
G14. $CH_3 + H + M \rightleftharpoons CH_4 + M$	2.4E + 22	−1.0	0.
G15. $CH_3 + H_2 \rightleftharpoons CH_4 + H$	2.9E + 12	3.1	8710.
G16. $CH_3 + CH_3 \rightleftharpoons C_2H_6$	2.0E + 13	0.0	0.
G17. $CH_3 + AsH_3 \rightleftharpoons AsH_2 + CH_4$	3.9E + 10	0.0	1650.

Note. Rate coefficients: $k = AT^{\beta} \exp(-E/RT)$ (gas phase reaction rates are in [mol/s/cm^3], E is in [cal/mol]).

matrix is replaced by the limit obtained when the species mass fractions are set to zero except that of the carrier gas which is set to one. The diffusion velocities are then given by

$$Y_i V_i = -\frac{W_i}{W_{n^{(g)}}} \mathscr{D}_{in^{(g)}} \nabla X_i, \quad i \neq n^{(g)},$$
$$Y_{n^{(g)}} V_{n^{(g)}} = -\sum_{i \neq n^{(g)}} Y_i V_i. \tag{16}$$

In the dilution limit, diagonal diffusion processes are thus obtained for the species in trace amounts and the diffusion velocity of the carrier gas simply ensures the mass conservation constraint (12). We will see in Section 4.2 that the dilution limit is not accurate.

In the present model we consider a total of $n^{(g)} = 15$ gas phase species, which are the gallium containing species $Ga(CH_3)_x$ ($x = 1, 2, 3$) and $Ga(CH_3)_xCH_2$ ($x = 0, 1, 2$), the arsenic containing species AsH_3, AsH_2, AsH, and As_2, and the carbon and hydrogen compounds CH_3, CH_4, C_2H_6, H, and H_2. These species participate in the chemical reactions presented in Table I [23]. Reactions G1–G2 correspond to the pyrolytic decomposition of trimethyl-gallium leading to the formation of dimethyl- and monomethyl-gallium. Demethylation of trimethyl- and dimethyl-gallium also occurs when atomic hydrogen abstracts a methyl radical leading to the formation of methane (reactions G3–G4). Reactions G5–G12 involve gallium-carbene species which are needed in the model in order to predict carbon incorporation levels in the epitaxial layer [23]. These reactions can be omitted from the kinetic mechanism without any significant change in the predicted growth rates. Recombination reactions of methyl and hydrogen radicals (reactions G13–G16) have been discussed extensively in combustion studies. Methyl radicals can also react with arsine leading to the formation of methane (reaction G17). Note that species AsH and As_2 are not present in any gas phase chemical reaction. As discussed later, these species are released at the substrate surface due to surface chemistry processes and are subsequently diffused and convected in the gas phase.

The gas phase molar production rate of the ith species is given by

$$\omega_i = \sum_{j=1}^{m^{(g)}} (\nu''_{ij} - \nu'_{ij}) \left(k'_j(T) \prod_{k=1}^{n^{(g)}} [\mathscr{X}_k]^{\nu'_{kj}} - k''_j(T) \prod_{k=1}^{n^{(g)}} [\mathscr{X}_k]^{\nu''_{kj}} \right), \tag{17}$$

where $m^{(g)} = 17$ is the number of gas phase reactions and where ν'_{ij} and ν''_{ij} are, respectively, the forward and reverse stoichiometric coefficients of the ith species in the jth reaction. In addition, $\mathscr{X}_k$ denotes the symbol of the kth gas phase species with concentration $[\mathscr{X}_k] = X_k(p/RT) = Y_k(\rho/W_k)$. The temperature dependent forward rate constant $k'_j(T)$ is modeled using a modified empirical Arrhenius expression

$$k'_j(T) = A_j T^{\beta_j} \exp\left(\frac{-E_j}{RT}\right), \qquad j = 1, ..., m^{(g)}. \tag{18}$$

The preexponential factor A_j, the temperature exponent

β_j, and the activation energy E_j are given in Table I. On the other hand, the reverse rate constant is given by the forward rate constant divided by the equilibrium constant, the latter being obtained from thermodynamic data [26].

The specification of boundary conditions at the substrate involves a detailed surface chemistry mechanism. More specifically, mass balance of gas phase species at the substrate surface yields

$$\rho Y_i(v_w + V_i) \cdot n = W_i \Omega_i, \quad i = 1, ..., n^{(g)}, \tag{19}$$

where v_w is the mass averaged flow velocity at the surface, n the normal to the surface pointing towards the gas phase, and Ω_i the surface molar production rate of the ith species. The velocity v_w is recovered from the sum of the $n^{(g)}$ equations (19) which yields

$$\rho v_w \cdot n = \sum_{i=1}^{n^{(g)}} W_i \Omega_i. \tag{20}$$

For the present operating conditions, the velocity v_w is of the order of one to two millimeters per second. Our numerical experiments show that this velocity can be neglected in the boundary conditions for the flow problem without significant changes in the numerical solution.

The surface chemistry mechanism used in this work [23] has been derived for a (110) surface orientation. This means that there is an equal number of gallium and arsenic atoms at the surface whose total concentration is $S_0 = 4.425 \times 10^{14}$ atm/cm^2. Other crystallographic orientations can be easily included in the numerical model by changing some surface reactions, as discussed in [23]. Apart from growth rate predictions, an important aspect in metalorganic CVD which is also addressed in the present model is the incorporation of undesired carbon atoms into the grown layer.

The chemical species are divided into four different phases. We consider $n^{(g)} = 15$ gas phase species, $n^{(s)} = 7$ surface species split into two different phases depending on whether the surface species occupies a gallium or an arsenic site, and, finally, $n^{(b)} = 2$ bulk species. The gallium sites can be occupied by the $n^{(G)} = 3$ surface species $H^{(G)}$, $CH_3^{(G)}$, $GaCH_3^{(G)}$, whereas the arsenic sites can be occupied by the $n^{(A)} = 4$ surface species $H^{(A)}$, $CH_3^{(A)}$, $AsH^{(A)}$, $As^{(A)}$. On the other hand, the bulk species are $GaAs^{(b)}$ and $GaC^{(b)}$, the latter being responsible for carbon incorporation into the epitaxial layer.

The concentration of the $n^{(s)}$ adsorbed species on the surface is conveniently described using site fractions σ_i, $1 \le i \le n^{(s)}$. The concentration (in mol/cm^2) of a surface species $\mathscr{S}_i$ is then given by

$$[\mathscr{S}_i] = \frac{S_0}{\mathscr{N}} \sigma_i, \tag{21}$$

where $\mathscr{N}$ is the Avogadro constant. We denote by S_G and S_A a free gallium or arsenic site, respectively. The site fraction of free gallium or arsenic sites, σ_G and σ_A, is then recovered from the overall site balance equations

$$\begin{aligned} \sigma_G &= 1 - (\sigma_{H^{(G)}} + \sigma_{CH_3^{(G)}} + \sigma_{GaCH_3^{(G)}}), \\ \sigma_A &= 1 - (\sigma_{H^{(A)}} + \sigma_{CH_3^{(A)}} + \sigma_{AsH^{(A)}} + \sigma_{As_2^{(A)}}). \end{aligned} \tag{22}$$

The surface mechanism presented in Table II [23] consists of $m^{(s)} = 30$ elementary irreversible reactions, which can be divided into four different types: adsorption, abstraction, surface recombination, and desorption. Adsorption reactions are described in the first part of Table II (reactions S1–S13). In this case, a gas phase species collides with one or two adjacent free sites, leading to the formation of an adsorbed species and, in the case of dissociative adsorption, to the release of some gas phase species as well. Adsorption reactions take the form

$$\mathscr{X}_i + \text{free site(s)} \rightharpoonup \text{products}, \tag{23}$$

where $\mathscr{X}_i$ is the chemical symbol of the ith gas phase species. The rate of progress for adsorption reactions is estimated using the kinetic theory collision rate modified by a coverage dependent sticking coefficient, i.e.,

$$q_{\text{ads}} = \frac{p}{\sqrt{2\pi W_i RT}} X_i s(\sigma). \tag{24}$$

Here, $s(\sigma)$ is the coverage dependent sticking coefficient given by

$$s(\sigma) = g(\sigma) \exp(-E/RT), \tag{25}$$

where $g(\sigma)$ is the fraction of free sites available for adsorption and E is the activation energy given in Table II. Note that in the present model we have $E = 0$ for all adsorption reactions; i.e., we have assumed the unit sticking coefficient at zero coverage. The form of function $g(\sigma)$ depends on the type and number of free sites involved. For single site adsorption, we have either $g(\sigma) = \sigma_G$ or $g(\sigma) = \sigma_A$, depending on the site type involved, and for two-site adsorption, we have $g(\sigma) = \sigma_G \sigma_A$.

Abstraction reactions (S14–S17 and S24) occur when a gas phase species reacts with a surface species, leading to the release of some gas phase species. Abstraction reactions take the form

$$\mathscr{X}_i + \mathscr{S}_j \rightharpoonup \text{products}, \tag{26}$$

TABLE II

Surface Reaction Mechanism

Reaction	A	E
S1. $H + S_G \rightarrow H^{(G)}$	—	0.
S2. $H + S_A \rightarrow H^{(A)}$	—	0.
S3. $CH_3 + S_G \rightarrow CH_3^{(G)}$	—	0.
S4. $CH_3 + S_A \rightarrow CH_3^{(A)}$	—	0.
S5. $GaCH_3 + S_G \rightarrow GaCH_3^{(G)}$	—	0.
S6. $Ga(CH_3)_2 + S_G \rightarrow GaCH_3^{(G)} + CH_3$	—	0.
S7. $Ga(CH_3)_3 + S_G \rightarrow GaCH_3^{(G)} + 2CH_3$	—	0.
S8. $GaCH_2 + S_G + S_A \rightarrow GaC^{(b)} + H_2$	—	0.
S9. $Ga(CH_3)CH_2 + S_G + S_A \rightarrow GaC^{(b)} + CH_3 + H_2$	—	0.
S10. $Ga(CH_3)_2CH_2 + S_G + S_A \rightarrow GaC^{(b)} + 2CH_3 + H_2$	—	0.
S11. $AsH + S_A \rightarrow AsH^{(A)}$	—	0.
S12. $AsH_2 + S_A \rightarrow AsH^{(A)} + H$	—	0.
S13. $AsH_3 + S_A \rightarrow AsH^{(A)} + H_2$	—	0.
S14. $CH_3 + H^{(G)} \rightarrow CH_4 + S_G$	—	0.
S15. $CH_3 + H^{(A)} \rightarrow CH_4 + S_A$	—	0.
S16. $H + CH_3^{(G)} \rightarrow CH_4 + S_G$	—	0.
S17. $H + CH_3^{(A)} \rightarrow CH_4 + S_A$	—	0.
S18. $H^{(G)} + CH_3^{(A)} \rightarrow CH_4 + S_G + S_A$	1.0E + 17	10000.
S19. $H^{(A)} + CH_3^{(G)} \rightarrow CH_4 + S_G + S_A$	1.0E + 17	10000.
S20. $H^{(G)} + H^{(A)} \rightarrow H_2 + S_G + S_A$	1.2E + 17	20000.
S21. $CH_3^{(G)} + CH_3^{(A)} \rightarrow C_2H_6 + S_G + S_A$	1.0E + 17	20000.
S22. $GaCH_3^{(G)} + AsH^{(A)} \rightarrow GaAs^{(b)} + CH_4 + S_G + S_A$	5.0E + 18	29300.
S23. $AsH^{(A)} + AsH^{(A)} \rightarrow As_2 + H_2 + 2S_A$	1.0E + 17	35000.
S24. $CH_3 + AsH^{(A)} \rightarrow As^{(A)} + CH_4$	—	20000.
S25. $As^{(A)} + As^{(A)} \rightarrow As_2 + 2S_A$	1.0E + 18	30000.
S26. $GaCH_3^{(G)} + As^{(A)} \rightarrow GaAs^{(b)} + CH_3 + S_G + S_A$	5.0E + 18	20000.
S27. $CH_3^{(G)} \rightarrow CH_3 + S_G$	1.0E + 12	20000.
S28. $CH_3^{(A)} \rightarrow CH_3 + S_A$	1.0E + 12	20000.
S29. $GaCH_3^{(G)} \rightarrow GaCH_3 + S_G$	1.0E + 14	40000.
S30. $AsH^{(A)} \rightarrow AsH + S_A$	1.0E + 14	40000.

Note. Rate coefficients: $k = A \exp(-E/RT)$. (surface reaction rates are in [mol/s/cm^2], E is in [cal/mol]).

where $\mathscr{S}_j$ denotes the symbol of the jth surface species. The corresponding rate of progress is written as

$$q_{\text{abs}} = \frac{p}{\sqrt{2\pi W_i RT}} \exp(-E/RT) X_i \sigma_j, \tag{27}$$

where the activation energy for abstraction, E, is again tabulated in Table II.

Surface species adsorbed on neighboring sites participate in bimolecular recombination reactions, leading to the removal of surface species and the formation of gas phase and possibly bulk species (reactions S18–S21, S23, and S25). Recombination reactions take the form

$$\mathscr{S}_i + \mathscr{S}_j \rightarrow \text{products}, \tag{28}$$

for which the rate of progress is written as

$$q_{\text{rec}} = A \exp(-E/RT)[\mathscr{S}_i][\mathscr{S}_j], \tag{29}$$

where the preexponential factor A and the activation energy for recombination E are given in Table II.

Finally, desorption of surface species (reactions S27–S30) occurs via the reaction

$$\mathscr{S}_i \rightarrow \text{gas phase species} + \text{free site}, \tag{30}$$

and the corresponding rate of progress is given by

$$q_{\text{des}} = A \exp(-E/RT)[\mathscr{S}_i]. \tag{31}$$

Using the above equations for the various rates of progress of the surface reactions, the surface production rate of any chemical species in any phase is given by

$$\Omega_i(X, \sigma) = \sum_{j=1}^{m^{(s)}} \nu_{ij}^{(s)} q_j(X, \sigma), \tag{32}$$

where $\nu_{ij}^{(s)}$ is the stoichiometric coefficient of the ith chemi-

cal species in the jth surface reaction. In addition, $X = (X_i)_{i\in[1,n^{(g)}]}$ denotes the mole fraction vector of the gas phase species and $\sigma = (\sigma_i)_{i\in[1,n^{(s)}]}$ denotes the site fraction vector. For later use and with obvious notation, the surface production rates are split into gas phase, surface, and bulk species surface production rates in the form

$$\Omega = (\omega^{(g)}, \Omega^{(s)}, \Omega^{(b)}), \tag{33}$$

where the vector $\Omega^{(g)}$ has $n^{(g)} = 15$ components, $\Omega^{(s)}$ has $n^{(s)} = 7$ components, and $\Omega^{(b)}$ has $n^{(b)} = 2$ components.

In order to compute $\Omega^{(g)}$ for the gas phase species, we need first to evaluate the site fraction vector σ. This is done by expressing mass conservation for the adsorbed species at the surface. Upon neglecting diffusion of adsorbed species along the surface, we may write

$$\Omega^{(s)}(X, \sigma) = 0. \tag{34}$$

Mass conservation of surface species thus yields a system of $n^{(s)}$ nonlinear equations which provides the site fractions as an implicit function of the gas phase mole fractions. As a result, Eqs. (19) and (34) completely specify the boundary conditions for the gas phase species.

Finally, the growth rate of the gallium arsenide layer [in cm/s] is given by

$$\mathscr{G} = k_{\mathrm{GaAs}}\Omega_{\mathrm{GaAs}^{(b)}}, \tag{35}$$

where $k_{\mathrm{GaAs}} = 27.19$ cm^3/mol is the molecular volume of gallium arsenide. On the other hand, the level of carbon incorporation [in atom/cm^3] is

$$\mathscr{C} = \frac{\mathscr{N}}{\mathscr{G}}\,\Omega_{\mathrm{GaC}^{(b)}}. \tag{36}$$

Note that $\Omega_{\mathrm{GaC}^{(b)}}$ is several orders of magnitude smaller than $\Omega_{\mathrm{GaAs}^{(b)}}$ so that it can be neglected in (35) when evaluating the growth rate of the epitaxial layer.

3. SOLUTION ALGORITHM

3.1. *Newton's Method and Adaptive Gridding Procedure*

The governing equations and boundary conditions described in Section 2 are discretized on a three-dimensional, tensor-product grid using a finite difference procedure. Centered differences are used except for the convective terms in the energy and species conservation equations which are discretized using a first-order, monotonicity preserving upwind scheme. For more details, we refer to [32].

For both the flow and the chemistry problems, the finite difference procedure yields a system of coupled nonlinear equations

$$F^{(r)}(U^{(r)}) = 0, \tag{37}$$

where the superscript $r = F, C$ refers to either the flow or the chemistry problem. Here, $F^{(r)}$ denotes the residuals of the discrete governing equations and boundary conditions, and $U^{(r)}$ denotes the discrete solution vector. Highly optimized FORTRAN libraries are used to evaluate the gas phase production rates [37] and the multicomponent transport coefficients [34]. The site fractions of the surface species are recovered from (34) using a standard Newton's method at each grid node over the substrate. Two to four iterations are typically required to achieve convergence to machine zero. The site fractions are subsequently used to form the boundary condition (19) for the gas phase species.

The residual equations (37) are solved over the three-dimensional CVD reactor using a modified damped Newton's method [38]

$$J^{(r)}(U^{(r),n+1} - U^{(r),n}) = -\lambda^n F^{(r)}(U^{(r),n}), \tag{38}$$

where $J^{(r)}$ is an approximation to the Jacobian matrix $\partial F^{(r)}/\partial U^{(r)}$ at $U^{(r),n}$ and λ^n is the nth damping parameter. The structure of the Jacobian matrix and its evaluation are discused in the next two sections. Convergence of the outer Newton iteration is achieved when the scaled norm of the update vector $U^{(r),n+1} - U^{(r),n}$ is reduced below a given tolerance, ranging from 10^{-5} (flow problem) to 10^{-9} (chemistry problem).

At each Newton step, an approximate solution to the linear system (38) is obtained with a Gauss–Seidel preconditioned Krylov-type iterative procedure, such as Bi-CGSTAB or GMRES. These linear system solvers have indeed met with significant success in numerical simulations of multidimensional combustion flows with detailed chemistry [32]. The Gauss–Seidel preconditioner is implemented in block form. It consists of a block tridiagonal solver for each vertical mesh row connecting the bottom and top boundaries (x direction) and a lower triangular sweep along the y and z directions (see Fig. 1). The effectiveness of this preconditioner relies upon the fact that, under typical operating conditions, minor transverse flow motion is obtained along the y direction while the predominant flow direction follows the z direction.

Finally, the numerical solution exhibits steep fronts where many components can undergo sharp variations. This is especially the case at the leading and trailing edges of the susceptor. As a consequence, an adaptive gridding procedure is used in order to cluster grid nodes in regions of high physical activity. The present approach equidistributes weight functions of the local gradient and curvature of the numerical solution [39]. Converged numerical solutions are obtained on a sequence of coarse to finest grids, until the solution profiles are adequately resolved. The finest grid contains $58 \times 12 \times 101$ nodes and the resulting Jacobian requires one gigabyte of computer memory. The grid in the transverse direction has been kept somewhat

coarse since only minor variations in the solution were observed transversally. For the two other directions, subsequent grid refinement has shown the grid independency of the solution.

3.2. *Structure of Jacobian Matrices*

The approximate Jacobian matrix plays a critical role in the numerical solution algorithm. Indeed, its accuracy determines the amount of information that is brought back to the Newton iteration through the update vector $U^{(r),n+1} - U^{(r),n}$ and thus drives the convergence rate of the solution method.

In order to reduce the CPU time, the Jacobian matrix is evaluated numerically rather than analytically whenever possible. The numerical evaluation of the Jacobian matrix is performed by splitting the mesh into independent groups. All the nodes pertaining to the same group can be perturbed simultaneously. If no second-order, cross derivatives are present in the governing equations, the Jacobian has seven block-diagonals and the mesh nodes (i, j, k) can be split into seven independent groups according to the value of the parameter

$$\alpha = i + 2j + 3k \mod 7. \tag{39}$$

Otherwise, the Jacobian contains 19 block-diagonals and the mesh nodes are then split into 27 independent groups according to the value of the parameter

$$\beta = i + 3j + 9k \mod 27. \tag{40}$$

For the flow problem, (39) can be used when the vorticity components are perturbed, while (40) must be used when perturbing either the velocity components or the temperature. For the chemistry problem, (39) is always used.

Another important aspect of the numerical evaluation of the Jacobian matrix is that most model parameters need only to be reevaluated at the perturbed nodes. The present approach follows the ideas discussed in [40]. For the flow problem, the heat transfer parameters needed for the temperature boundary conditions are only reevaluated at the perturbed nodes and only if the temperature is being perturbed. For the chemistry problem, the transport coefficients and the gas phase production rates are only evaluated at the perturbed nodes. This approach reduces considerably the CPU time required to form a Jacobian.

For the flow problem, an additional simplification is used which reduces considerably the memory requirements (see [30] for more details). Although a 27-point stencil is used to form the approximate Jacobian matrix, only the seven block-diagonals corresponding to the nearest neighbor coupling in the stencil are retained when solving the linear system (38). With this approach, only a slight degradation in the convergence rate of Newton's method is obtained, while the storage requirements are divided by a factor of almost three.

For the flow problem, the Jacobian is always evaluated numerically. For the chemistry problem, however, it is critical that the approximate Jacobian matrix has as much information as possible regarding the surface chemistry processes. In this case, we use the following hybrid approach. The matrix $J^{(C)}$ is split into

$$J^{(C)} = J^{(C,\text{surf})} + \Im^{(C)}, \tag{41}$$

where $J^{(C,\text{surf})}$ denotes the part of $J^{(C)}$ associated with the surface chemistry processes. In the present solution algorithm, the matrix $\Im^{(C)}$ is still evaluated numerically, but the matrix $J^{(C,\text{surf})}$ is evaluated analytically, as discussed in the next section.

3.3. *Analytical Treatment of the Surface Chemistry*

The analytical Jacobian procedure requires the evaluation of the matrix $d\Omega^{(g)}/dX$ with $n^{(g)}$ rows and columns. We restate that X denotes the vector of size $n^{(g)}$ formed by the gas phase species mole fractions and that $\Omega^{(g)}$ denotes the vector of size $n^{(g)}$ formed by the gas phase species surface production rates. We also restate that we have

$$\Omega^{(g)} = \Omega^{(g)}(X, \sigma(X)), \tag{42}$$

where the site fractions are defined implicitly as functions of the mole fractions through the relations $\Omega^{(s)}(X, \sigma(X)) = 0$. Differentiation of (42) yields

$$\frac{d\Omega^{(g)}}{dX} = \frac{\partial \Omega^{(g)}}{\partial X} + \frac{\partial \Omega^{(g)}}{\partial \sigma}\frac{d\sigma}{dX}. \tag{43}$$

Both the $n^{(g)} \times n^{(g)}$ matrix $(\partial\Omega^{(g)}/\partial X)$ and the $n^{(g)} \times n^{(s)}$ matrix $(\partial\Omega^{(g)}/\partial\sigma)$ can be evaluated analytically using the expressions for the surface reaction rates of progress described in Section 2.3. On the other hand, the $n^{(s)} \times n^{(g)}$ matrix $(d\sigma/dX)$ is obtained by differentiating (34) with respect to X, yielding

$$\frac{d\sigma}{dX} = -\left(\frac{\partial \Omega^{(s)}}{\partial \sigma}\right)^{-1}\frac{\partial \Omega^{(s)}}{\partial X}, \tag{44}$$

and the right member can be again evaluated analytically from Section 2.3. Finally, since the dependent unknowns are the species mass fractions $Y_1, ..., Y_{n^{(g)}-1}$ (recall that the carrier gas mass fraction is recovered from $\sum_{i=1}^{n^{(g)}} Y_i = 1$)

instead of the species mole fractions, we also need to form the quantities

$$\frac{\partial X_i}{\partial Y_j} = \frac{W}{W_j}\left(\delta_{ij} - X_i\left(1 - \frac{W_j}{W_{n^{(g)}}}\right)\right), \quad 1 \le i \le n^{(g)}, 1 \le j \le n^{(g)} - 1. \tag{45}$$

3.4. *Sensitivity Analysis*

The use of Newton's method for the numerical solution of the governing equations provides a very efficient and elegant means to perform sensitivity analysis [41]. Sensitivity analysis is, in turn, an important numerical tool for probing the influence of physical parameters on model predictions and may thus provide useful information for further model developments and experimental design. At the most basic level, first-order sensitivity coefficients are partial derivatives of the numerical solution with respect to some parameter. The nonlinear equations (37) are rewritten in the form

$$F(U; \alpha) = 0, \tag{46}$$

where we have omitted the superscript r and where $\alpha = (\alpha_i)_{1 \le i \le M}$ denotes the parameter vector. Differentiation of (46) yields

$$J\frac{\partial U}{\partial \alpha_k} = -\frac{\partial F}{\partial \alpha_k}, \quad k = 1, ..., M, \tag{47}$$

where J is the Jacobian matrix. The first-order sensitivities $\partial U/\partial \alpha_k$ are formed only when a converged numerical solution has been obtained on the finest grid. In practice, the last numerical Jacobian evaluated in Newton's method is used in (47). For a perturbation analysis resulting from the use of an approximate Jacobian matrix, we refer to [41].

In this work, we are interested in predicting the effects of the variation of the parameter vector α on the surface production rates of the bulk species $\Omega^{(b)}$. This leads to the following derived sensitivity coefficients

$$\frac{d}{d\alpha_k}\Omega^{(b)}(X, \sigma; \alpha) = \frac{\partial \Omega^{(b)}}{\partial X}\frac{\partial X}{\partial \alpha_k} + \frac{\partial \Omega^{(b)}}{\partial \sigma}\frac{\partial \sigma}{\partial \alpha_k} + \frac{\partial \Omega^{(b)}}{\partial \alpha_k}. \tag{48}$$

The quantity $\partial X/\partial \alpha_k$ is recovered from the first-order sensitivity coefficients. The quantity $\partial \sigma/\partial \alpha_k$ is evaluated by differentiating the relation $\Omega^{(s)}(X, \sigma; \alpha) = 0$. Finally, the quantity $\partial \Omega^{(b)}/\partial \alpha_k$ is usually zero, unless $\Omega^{(b)}$ explicitly depends on α_k.

Another approach in sensitivity analysis consists in first perturbing the parameters, then obtaining a new converged solution, and finally forming the appropriate divided difference quotients to evaluate the sensitivities. In the one-dimensional case, the Jacobian matrix is block tridiagonal and the linear system (47) can be solved with a direct method in an efficient form [41]. In this case, the "differential" approach (46)–(48) is thus preferable to evaluate the sensitivities. In the multidimensional case, solving the linear system (47) with an iterative method might not yield accurate enough first-order sensitivities while using a direct solver might require extremely large computer resources. In this case, the "perturbation" approach is retained in order to form the sensitivities.

4. NUMERICAL RESULTS AND DISCUSSION

In this section we use the physical models and the solution algorithm described in the previous sections in order to study numerically a typical metalorganic CVD reactor. The numerical results have been obtained on an IBM RS 6000 (model 590) computer. The computations required up to one gigabyte of computer memory and took 1–10 h of CPU time. Five to ten Newton iterations were generally required with near optimal convergence rates.

We consider a three-dimensional, horizontal channel reactor as illustrated in Fig. 1. The reactor is 10 cm long, 3 cm high, and 7.2 cm wide and is operated at atmospheric pressure. The substrate is 1 cm long with its leading edge located 4 cm downstream from the inflow boundary. The substrate is set on a susceptor at temperature 948 K which extends up to the outflow boundary of the reactor. A mixture of trimethyl-gallium (in short, TMG) and arsine diluted in hydrogen is fed to the reactor with a volumetric flow rate of 5 l/min at standard conditions (in short, SLM). The inlet partial pressure of TMG and arsine is $p_{\mathrm{TMG}} = 1.8 \times 10^{-4}$ atm and $p_{\mathrm{AsH_3}} = 3.3 \times 10^{-3}$ atm. These operating conditions were chosen to match the ones used in previous experimental work [42]. They define the base case for the present work.

4.1. *Flow Field and Temperature Distribution*

The temperature distribution inside the three-dimensional CVD reactor is illustrated in Fig. 2. A linear temperature variation along the vertical direction is established at about 3 cm downstream from the leading edge of the susceptor. One can also see from Fig. 2 that the temperature at the top wall is higher near the symmetry plane than near the side walls due to the increased effectiveness of radiation heat transfer from the susceptor in this area.

Under the present operating conditions, mixed convection flow patterns arise inside the CVD reactor. The main flow motion corresponds to a fully developed flow along the reactor (the z direction in Fig. 1) which is accelerated due to the temperature increase in the region above the susceptor. The three-dimensional structure of the flow field can be analyzed in terms of return flows and longitudinal rolls. Return flows form in a transition zone separating an

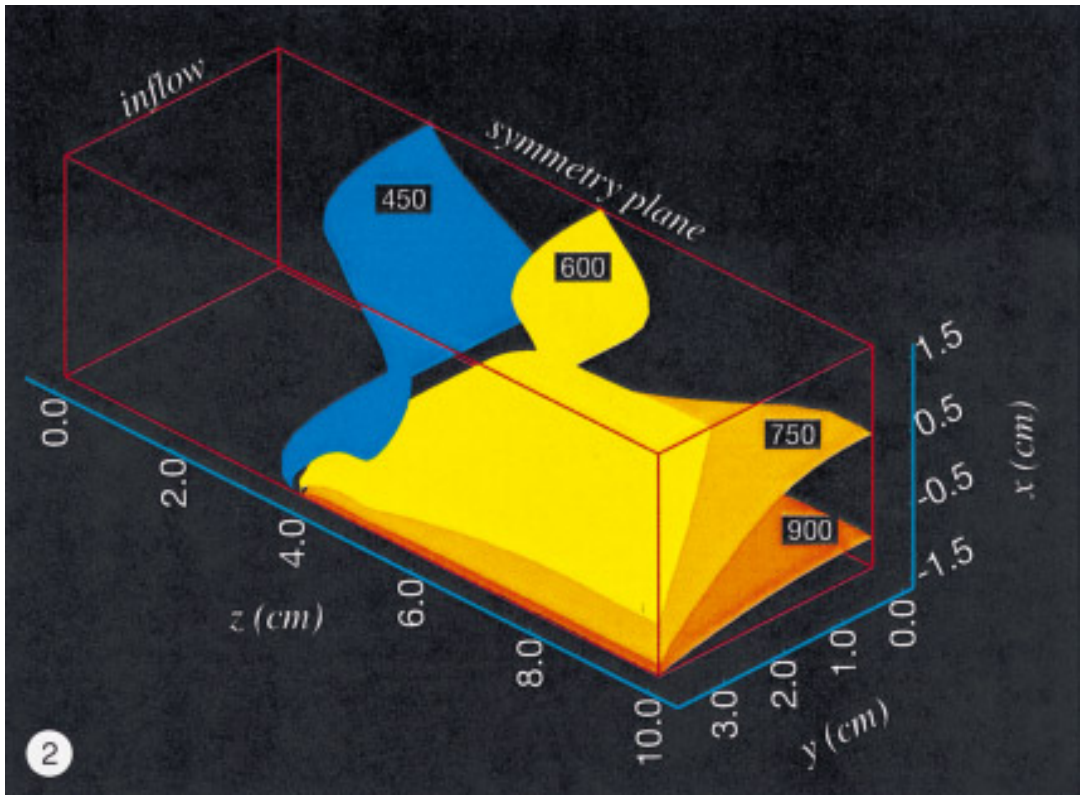

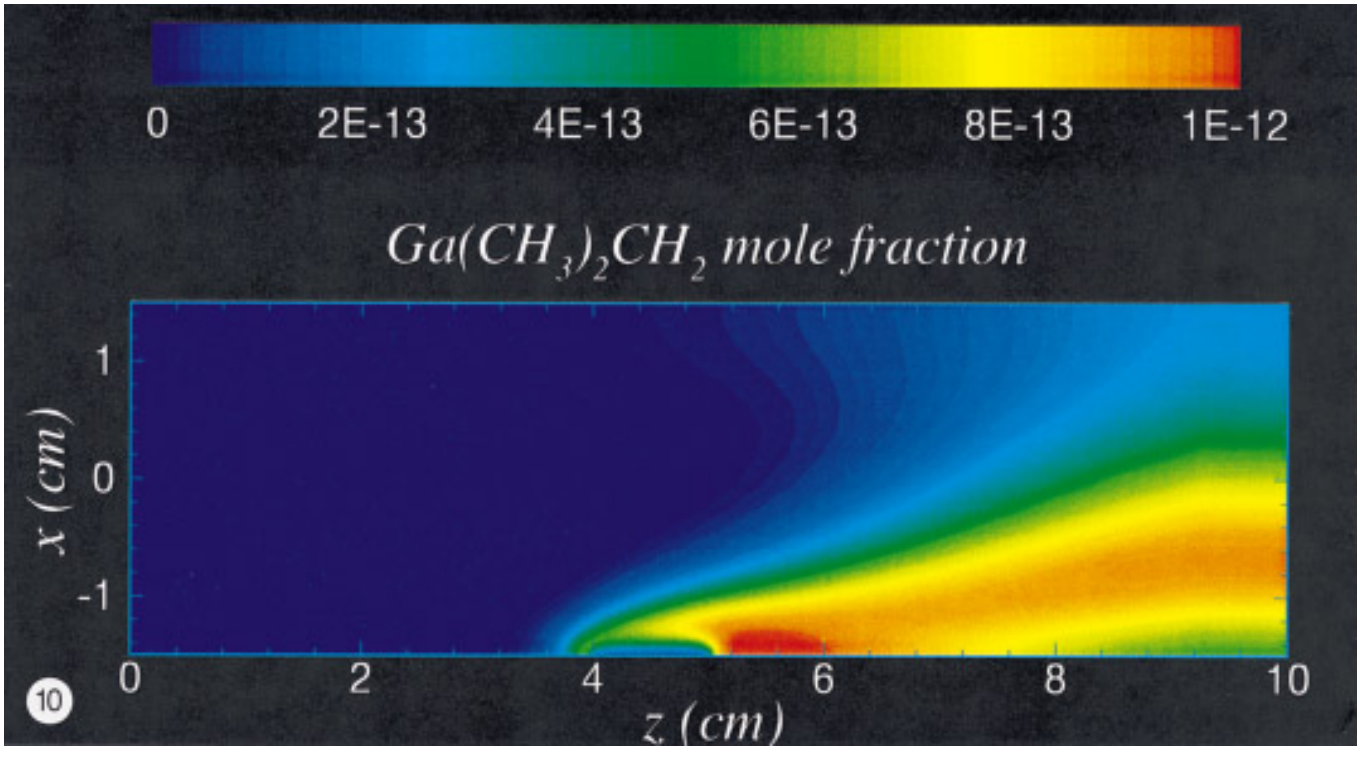

FIG. 2. Isotherms inside the three-dimensional CVD reactor. Susceptor temperature: 948 K; inlet flow rate: 5 SLM; partial pressure of TMG: 1.8×10^{-4} atm; partial pressure of arsine: 3.3×10^{-3} atm; total pressure: 1 atm.

FIG. 10. Isopleths for $Ga(CH_3)_2CH_2$ mole fraction at the reactor symmetry plane. Growth conditions as in Fig. 2.

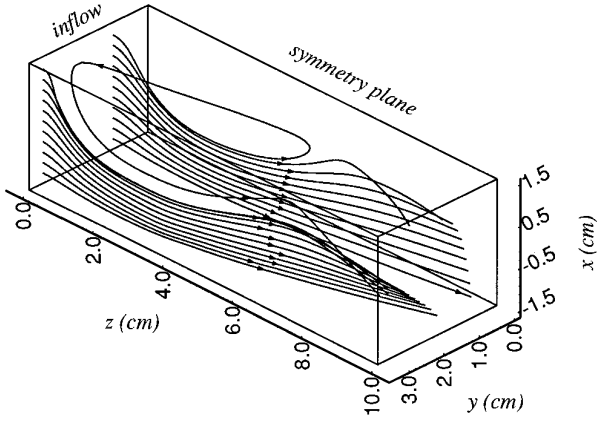

FIG. 3. Streamlines inside the three-dimensional CVD reactor illustrating the return flow and the longitudinal roll. Growth conditions as in Fig. 2.

isothermal entrance region from a differentially heated zone. They arise typically above the leading edge of the susceptor near the top wall and consist in rolls spinning around an axis parallel to the transverse direction (the y direction in Fig. 1). The onset of return flows in CVD reactors can be analyzed with two-dimensional models and has been the subject of extensive research [8, 43]. Return flows generally have a minor impact on the spatial variations of the growth rate, but may increase the residence time of growth precursors and dopants, thus yielding broader heterojunctions [10]. In addition, the presence of return flows prevents the use of simplifying numerical techniques such as parabolic marching procedures along the reactor. On the other hand, longitudinal rolls can only be predicted using three-dimensional models. They correspond to flow motion spinning around an axis parallel to the main flow direction (the z direction in Fig. 1). Longitudinal rolls may affect transverse film thickness uniformity [13, 14].

For the present reactor configurations, return flows and longitudinal rolls are predicted by the numerical model. Streamlines inside the CVD reactor are presented in Fig. 3. They clearly show the presence of a return flow above the leading edge of the susceptor. The return flow is coupled to two symmetric longitudinal rolls (only one appears in Fig. 3). Due to the longitudinal roll, precursor species formed near the symmetry plane of the reactor are brought toward the side walls of the reactor. This process reduces the transverse non-uniformity of the film thickness distribution. Note that the inlet velocity boundary condition prevents the return flow from exiting at the inlet (see Figs. 3–5). This may result in a physically unrealistic velocity profile near the inlet. The present inlet velocity boundary condition has been chosen for the sake of simplicity and demonstration purposes. More sophisticated boundary conditions specifying for instance the pressure drop can also be used, but their study is beyond the scope of this paper.

Further insight into the flow field and temperature distribution at the symmetry plane is given in Fig. 4. Due to the relatively low flow rate (5 SLM), heat conduction is sufficiently fast with respect to convection. As a result, the low temperature core convected by the main flow motion penetrates only moderately inside the region above the hot susceptor. On the other hand, the return flow is clearly illustrated by the velocity profiles. Figure 5 next shows the influence of susceptor temperature on the return cell. For high susceptor temperatures (1198 K), the return cell is confined to a small region which only extends for about 1 cm above the susceptor. For low susceptor temperatures (698 K), the return cell extends much further downstream (up to 3.5 cm from the leading edge of the susceptor). The influence of the flow rate on the temperature distribution is illustrated in Fig. 6. At low flow rates (2 SLM), heat conduction inside the reactor dominates over convective processes and the 700 K isotherm reaches the top wall. At high flow rates (8 SLM), convection becomes more important and two thermal boundary layers develop, one from the susceptor and one from the slowly heating top wall. The merging of these two layers gives rise to the so-called ''cold finger'' phenomenon [10]. Due to thermal diffusion processes, the cold finger contains heavy source reactants which are thus convected further downstream. The availability of these fresh precursors near the trailing

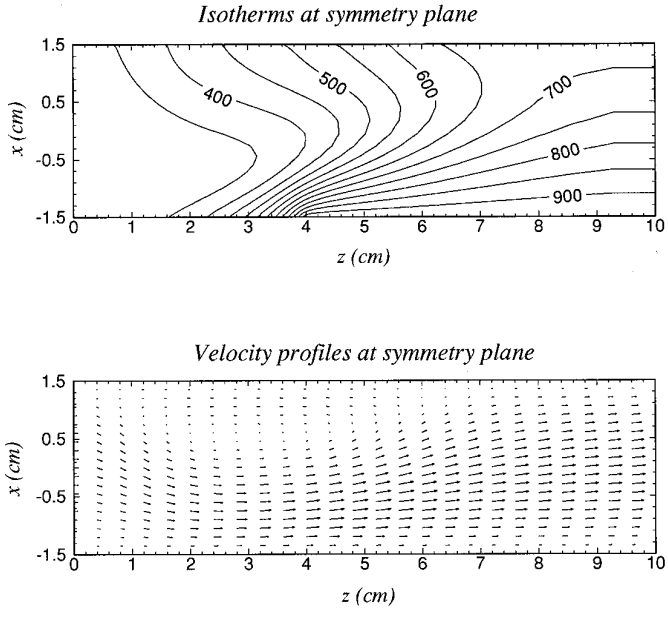

FIG. 4. Isotherms and velocity profiles at the symmetry plane. Growth conditions as in Fig. 2.

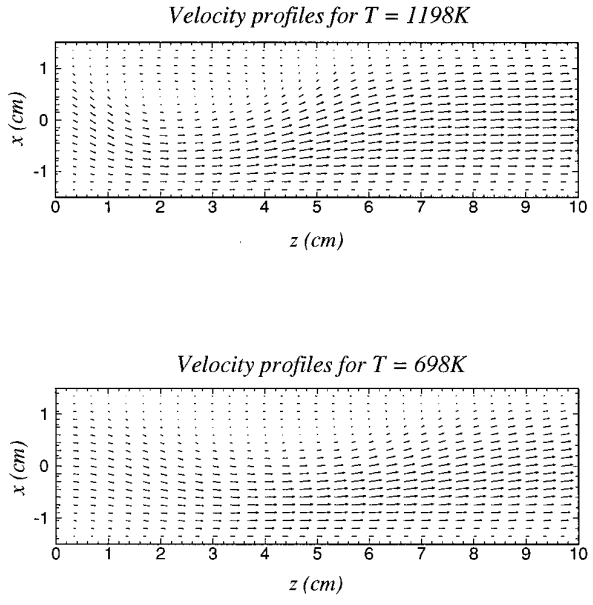

FIG. 5. Velocity profiles at the symmetry plane for two different susceptor temperatures; 698 K (lower figure) and 1198 K (upper figure). Other growth conditions as in Fig. 2.

edge of the substrate may enhance longitudinal film thickness uniformity.

4.2. *Detailed Chemistry Results*

The transverse and longitudinal variation of the growth rate and of the carbon incorporation level are illustrated in Fig. 7 for the present operating conditions. Both quantities decrease away from the symmetry plane and are locally maximal at the leading and trailing edges of the substrate. Note that carbon levels are actually higher at the trailing edge of the substrate than at its leading edge. This result is due to the fact that gallium-carbene species are primarily formed in the downstream region of the CVD reactor. This point will be further illustrated in Fig. 10.

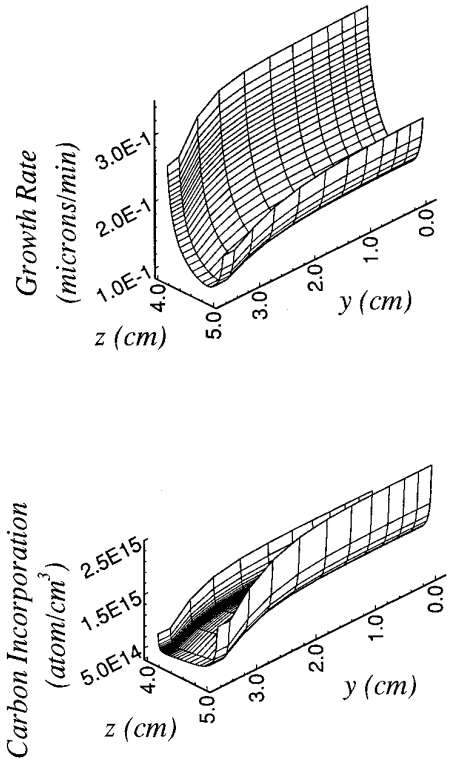

FIG. 7. Growth rate (μm/min) and carbon incorporation levels (atom/cm^3) on the substrate. Growth conditions as in Fig. 2.

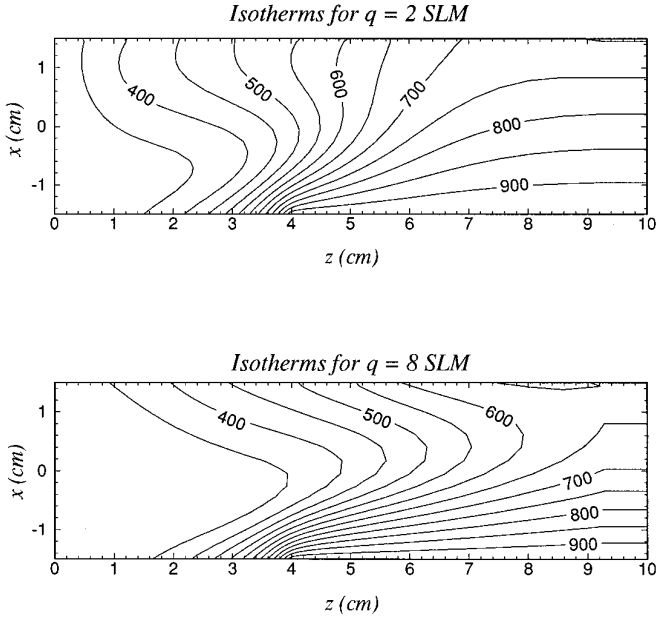

FIG. 6. Isotherms at the symmetry plane for two different inlet flow rates; 2 SLM (upper figure) and 8 SLM (lower figure). Other growth conditions as in Fig. 2.

Further insight into the three-dimensional, gas phase chemical processes is given in Figs. 8 and 9, where the spatial variation of several species mole fractions is presented at the bottom plane of the reactor. Figure 8 first shows the depletion of trimethyl-gallium above the substrate where it reaches a minimum mole fraction of $X_{\mathrm{TMG}} = 4.8 \times 10^{-8}$. Monomethyl-gallium and methane are primarily produced above the substrate, the former from the pyrolytic decomposition of TMG and the latter mainly from surface processes. On the other hand, ethane is primarily produced by gas phase reactions through the recombination of methyl radicals. Figure 9 focuses on the four arsenic containing species considered in the model. Arsine is depleted above the substrate where its minimum mole fraction is $X_{\mathrm{AsH_3}} = 1.6 \times 10^{-5}$. Species AsH_2 is produced by gas phase reactions in a region located downstream from the substrate. In addition, AsH and As_2 are released

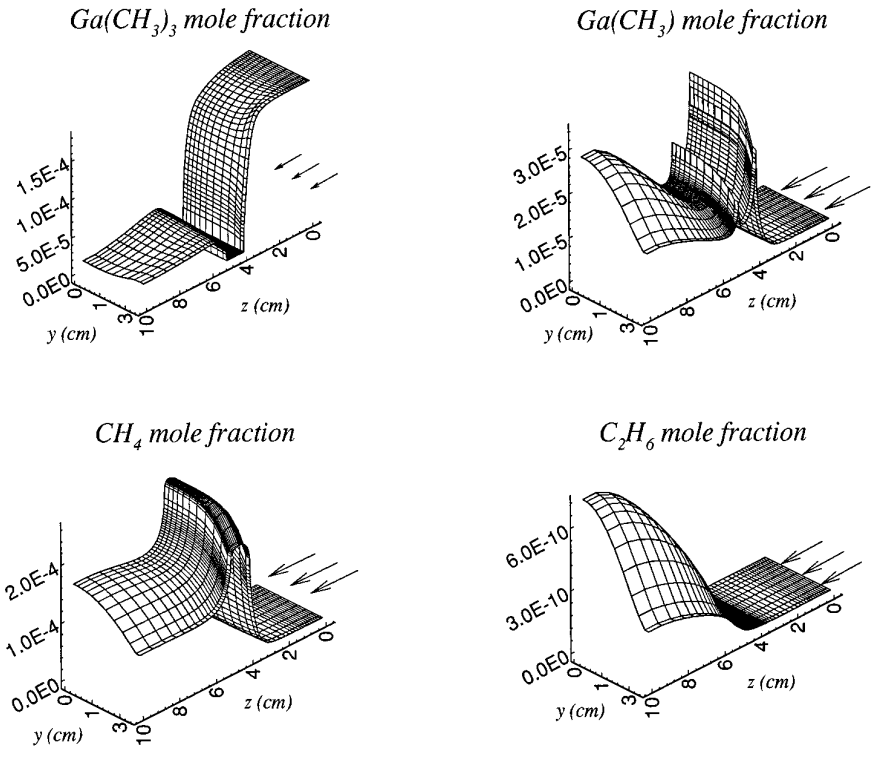

FIG. 8. Surface contours for $Ga(CH_3)_3$, $Ga(CH_3)$, CH_4, and C_2H_6 mole fraction at the reactor bottom plane. Growth conditions as in Fig. 2.

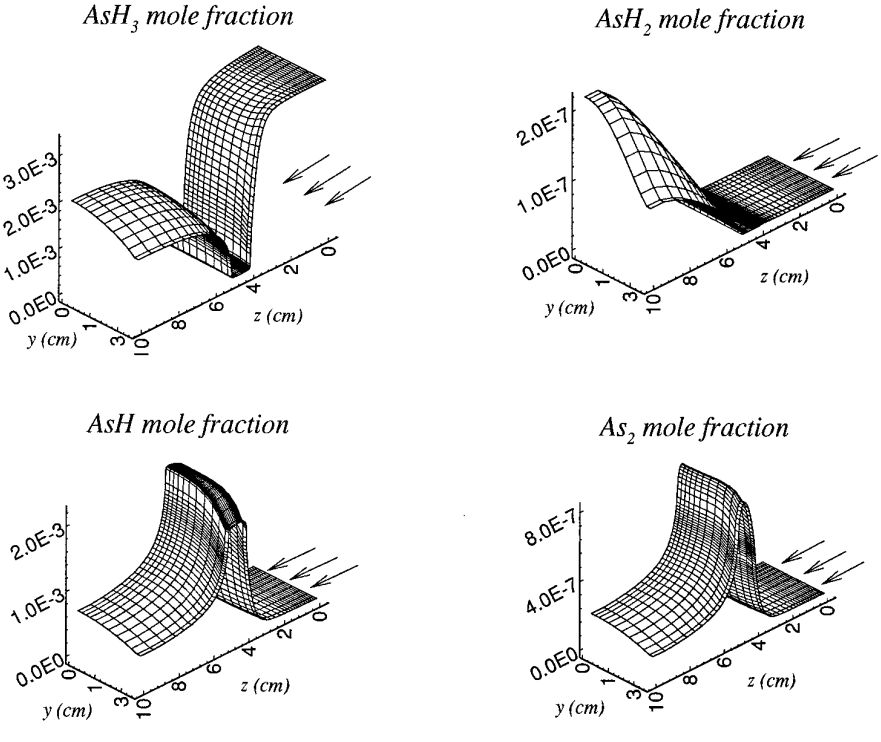

FIG. 9. Surface contours for AsH_3, AsH_2, AsH, and As_2 mole fraction at the reactor bottom plane. Growth conditions as in Fig. 2.

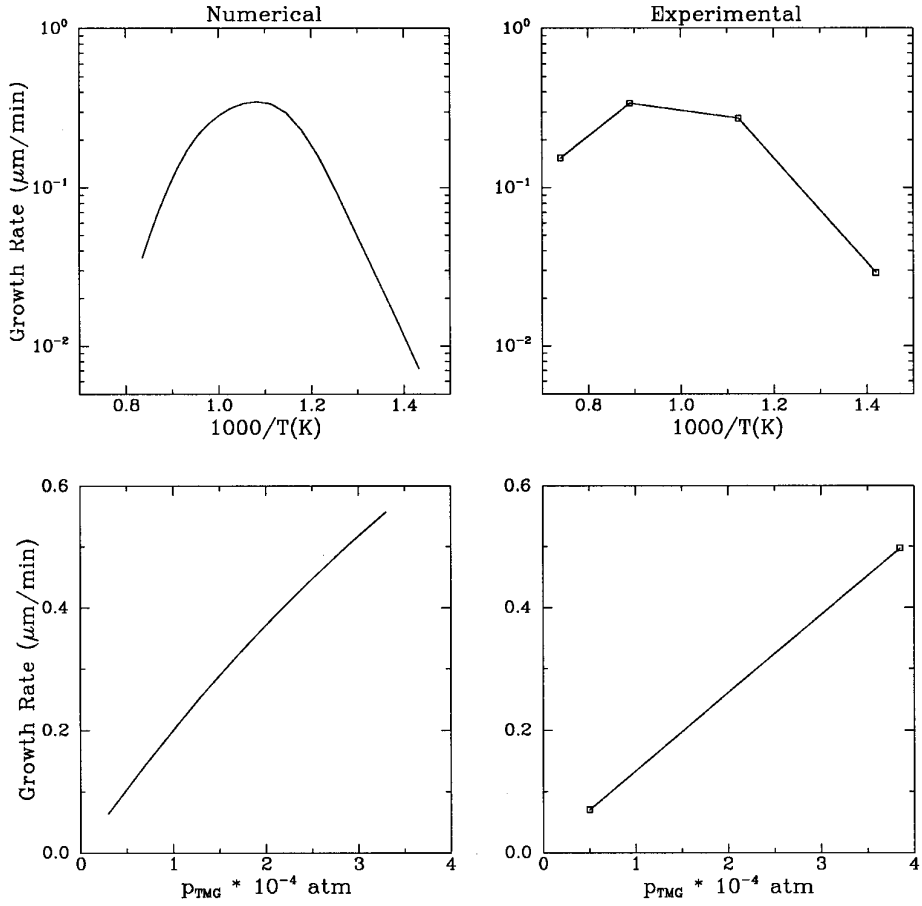

FIG. 11. Comparison of numerical and experimental [42] growth rate predictions for various susceptor temperatures and for various TMG partial pressures. Other growth conditions as in Fig. 2.

into the gas phase due to surface processes and are then diffused and convected downstream. Figure 10 next presents isopleths for the mole fraction of $Ga(CH_3)_2CH_2$ at the symmetry plane. This species has the largest concentration among the gallium-carbene species considered in this model. It is formed through gas phase chemical reactions, primarily in a region downstream from the depletion zone. Due to diffusion processes, however, this species is also present near the trailing edge of the substrate. This phenomenon leads to larger carbon incorporation levels in this area, as already illustrated in Fig. 7.

Predicted growth rates of GaAs at different susceptor temperatures and for different inlet TMG partial pressures are next presented in Fig. 11. In this figure, the experimental results of [42] are also plotted. At low temperatures, the growth process is controlled by the kinetics of the surface reactions and is rather slow. In the mid temperature range, the process becomes mass diffusion limited and is fairly insensitive to the susceptor temperature. At high temperatures, desorption reactions become dominant and transport processes of precursor species from the gas phase can no longer supply growth precursors, thus leading to a sharp decrease of the growth rate. On the other hand, Fig. 11 shows an almost linear dependence of the growth rate on p_{TMG} for a susceptor temperature of 948 K. This is to be expected since for this temperature the growth rate is limited by the diffusion of the less abundant species (TMG) to the depletion surface.

Predicted carbon incorporation levels as a function of temperature and V/III element ratio are presented in Fig. 12. The numerical results reproduce the trends reported in [23] for a different reactor configuration. Both models predict an increased level of carbon incorporation with higher susceptor temperatures as a result of enhanced production of methyl radicals which can attack unreacted TMG to form $Ga(CH_3)_2CH_2$ (see reaction G5 in Table I). In addition, decreasing the partial pressure of TMG leads to lower amounts of carbon being incorporated. This latter result was also observed experimentally by using photoluminescence [44].

In order to further illustrate the surface mechanism, we present in Fig. 13 the surface species site fractions along

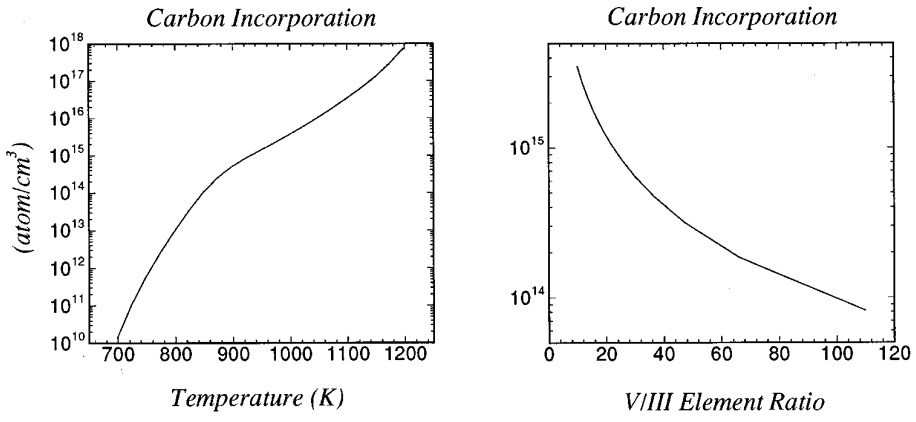

FIG. 12. Predicted carbon incorporation levels as a function of susceptor temperature and V/III element ratio. Other growth conditions as in Fig. 2.

the substrate for various susceptor temperatures. For simplicity, the value of the site fractions at the leading edge of the substrate is used. Both gallium and arsenic sites are almost completely covered in the low to mid temperature range. At high temperatures, however, the surface coverage decreases significantly due to enhanced recombination and desorption reactions. The numerical results reproduce those reported in [23], except for the hydrogen species $H^{(G)}$ and $H^{(A)}$. Indeed, only the present model includes thermal diffusion which results in light species having larger concentrations near the hot substrate and thus predicts higher levels of hydrogen adsorption.

We next consider the influence of susceptor temperature on longitudinal growth rate uniformity. Figure 14 presents the variation of the normalized growth rate along the substrate at the symmetry plane for three different susceptor temperatures. The growth rate is normalized by its value at the leading edge of the substrate. At low and high temperatures (798 and 1198 K), the growth rate exhibits a very minor variation along the substrate. At mid temperatures (998 K) where the growth process is mass diffusion controlled, the longitudinal variation of the growth rate becomes more important. Indeed, a larger amount of source reactants are available at the leading and trailing edges of the substrate due to upstream or downstream diffusion.

The impact of transport algorithms on model predictions is illustrated in Fig. 15. In this figure we present the growth rate which results from three different formulations for the species diffusion velocities. The first case corresponds to the most detailed formulation: thermal diffusion is in-

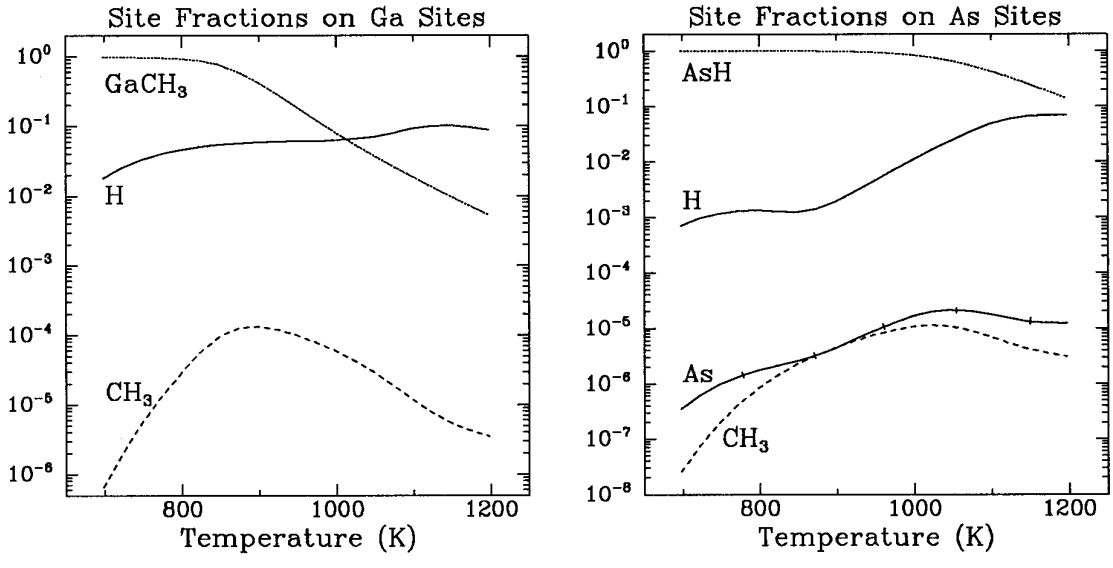

FIG. 13. Predicted site fractions at the leading edge of the substrate for various susceptor temperatures. Other growth conditions as in Fig. 2.

cluded and the flux diffusion matrix is evaluated from (14). The second case neglects thermal diffusion. Finally, the third case retains thermal diffusion but uses the dilution limit (16) for the flux diffusion matrix. Figure 15 shows that only the detailed transport formulation can accurately describe the growth process. Thermal diffusion drives heavy gaseous precursors away from the hot depletion zone and thus leads to lower growth rates and carbon incorporation levels. In the present model, the neglect of thermal diffusion can cause overestimation of the growth rate by 32% and of the carbon incorporation levels by 53%. In addition, our numerical results show the relevance of the off-diagonal diffusion coefficients in accurate CVD modeling. The use of the dilution limit can cause overestimation of the growth rate by 12% and of the carbon incorporation levels by 9%.

Finally, with the large number of parameters involved in the specification of the detailed chemistry model, it is useful to perform a sensitivity analysis to evaluate the influence of these parameters on model predictions. Sensitivity analysis can also motivate further experimental work by providing insight into the critical reaction steps in the growth process. Our numerical results show that gas phase chemistry only plays a minor role in film thickness distribution. For instance, the inclusion of gas phase chemical reactions into the model only lowers the predicted average growth rate by 3.4%. For a discussion of the influence of gas phase chemistry on carbon incorporation, we refer to

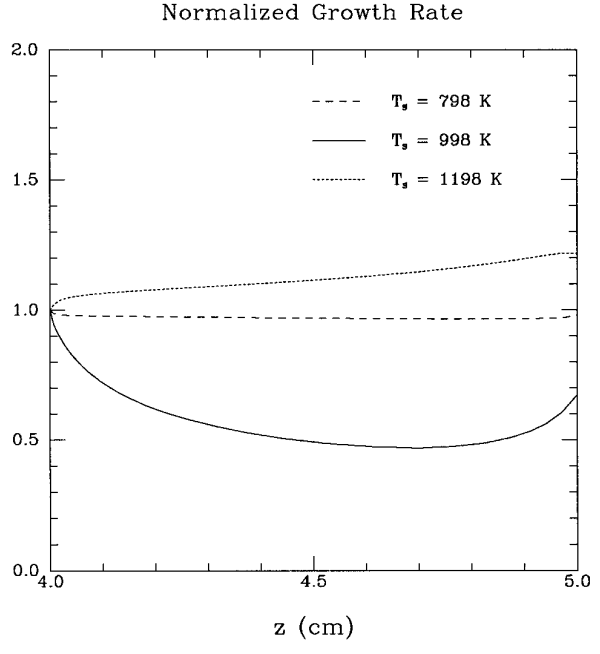

FIG. 14. Normalized growth rate along the substrate at the reactor symmetry plane for three susceptor temperatures; 798 K (– –), 998 K (———), and 1198 K (...).

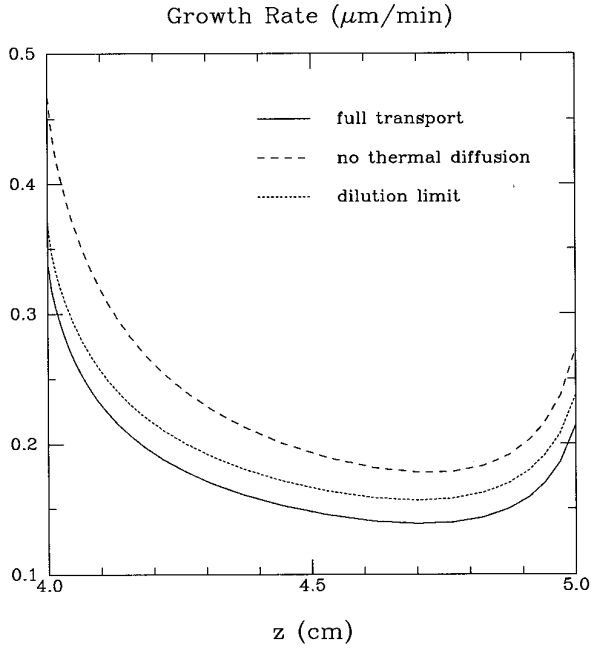

FIG. 15. Growth rate predictions along the substrate at the reactor symmetry plane for three different transport models; full transport (———), no thermal diffusion (– –), and dilution limit for the species diffusion coefficients (...).

[23]. As a result, the present sensitivity analysis focuses on the surface chemistry mechanism. We consider the activation energies of the surface reactions as parameters and we want to study the influence of these parameters on the surface production rate of the two bulk species, $GaAs^{(b)}$ and $GaC^{(b)}$. The activation energy provides a measure of the reactivity of the corresponding surface reaction, but other parameters in the system could have been chosen as well.

We evaluate the normalized sensitivity coefficients $RT\partial \ln \Omega_i^{(b)}/\partial E_k$ at the leading edge of the substrate. Sensitivities are presented in Table III for both bulk species with reaction numbers referring to Table II. For gallium arsenide, the largest sensitivity in Table III corresponds to

TABLE III

Bulk Species Sensitivities to Surface Reaction Activation Energies (reaction numbers refer to Table II.)

$GaAs^{(b)}$	Reaction	$GaC^{(b)}$	Reaction
−6.0E − 1	S22	−3.0E − 1	S30
4.7E − 1	S29	2.7E − 1	S11
−4.6E − 1	S5	−1.8E − 1	S29
3.4E − 2	S30	1.8E − 1	S5
−3.0E − 2	S11	1.5E − 1	S22
−1.0E − 2	S7	3.0E − 2	S13
−3.4E − 3	S13	2.4E − 2	S1

surface recombination of $GaCH_3^{(G)}$ and $AsH^{(A)}$ to form $GaAs^{(b)}$ (reaction S22). It is also interesting to notice the importance of reactions S29 and S5 corresponding, respectively, to desorption and adsorption of monomethyl-gallium. The adsorption and desorption of AsH (reactions S11 and S30) also plays a critical role. The adsorption of the source reactants, $Ga(CH_3)_3$ and AsH_3, is somewhat less sensitive (reactions S7 and S13). For carbon incorporation, the critical steps are the desorption and adsorption of AsH and $GaCH_3$. The desorption reactions have a negative sensitivity since they tend to increase the free sites at the surface and thus favor the two-site adsorption of the gallium-carbene species. The same remark holds for reaction S22 which leads to the production of two free sites at the surface. While a more extensive sensitivity analysis goes beyond the scope of this study, it effectively emphasizes the critical reaction steps in the surface chemistry mechanism.

5. CONCLUSIONS

In this paper we have derived a numerical model for a three-dimensional, horizontal channel, chemical vapor deposition reactor in order to simulate gallium arsenide growth from trimethyl-gallium and arsine source reactants. The present model is able to reproduce several key features of the CVD process, including the onset of return flows and longitudinal rolls, the ''cold finger'' phenomenon, and the influence of susceptor temperature and trimethyl-gallium partial pressure on growth rate and carbon incorporation. The numerical model also shows that under the present operating conditions the growth rate does not depend significantly on the details of the gas phase chemistry mechanism but it strongly depends on the surface chemistry. Gas phase chemistry is, however, needed to simulate carbon incorporation through adsorption of gallium-carbene species. An essential feature of the present work is also the accurate treatment of precursor species transport in the gas phase. It is indeed critical for accurate model predictions to use species diffusion velocities that account for both thermal diffusion and multicomponent diffusion processes. In this context, a computationally effective approach is then to use the theory of iterative transport algorithms.

APPENDIX A: HEAT TRANSFER MODEL AT REACTOR WALLS

In this appendix we briefly describe the boundary condition used to determine the temperature on the reactor quartz walls. We consider a wall element as illustrated in Fig. 1. The temperature boundary condition expresses its energy balance in the form

$$\sum_{i=1}^{6} q_i \delta s_i = 0, \tag{A.1}$$

where δs_i is the surface of the ith face of the wall element and q_i the corresponding heat flux from the wall element. The values of δs_i result from the mesh spacing used to discretize the CVD reactor, and the thickness of the quartz wall is set to 2.5 mm. For the outer face, the heat flux includes radiation to the surroundings and cooling by the surrounding air. For the inner face, radiation from the susceptor and conduction from the hot gases inside the reactor are considered, while radiation to the inner part of the reactor walls from the other facing walls is neglected. Finally, for the four lateral faces, the heat flux corresponds to heat conduction through the wall.

The inner radiation flux is expressed as

$$q_{\mathrm{rad,i}} = \sigma \sum_j F_j(\varepsilon_{\mathrm{w}} T_{\mathrm{w}}^4 - \varepsilon_{\mathrm{g}} T_{\mathrm{s}}^4), \tag{A.2}$$

where $\sigma = 5.669 \times 10^{-5}$ is the Stefan–Maxwell constant (in cgs units), the index j refers to an elementary surface of the susceptor, F_j is the configuration factor for the jth element, ε_{g} is the susceptor emissivity ($\varepsilon_{\mathrm{g}} = 0.78$ for a graphite susceptor), T_{s} is the susceptor temperature, ε_{w} is the wall emissivity ($\varepsilon_{\mathrm{w}} = 0.2$ for quartz), and T_{w} is the local wall temperature. The evaluation of the configuration factor involves integration over the specific geometry of the emitting and receiving surface [45]. On the other hand, the outer radiation flux is given by

$$q_{\mathrm{rad,o}} = \sigma \varepsilon_{\mathrm{w}} (T_{\mathrm{w}}^4 - T_\infty^4), \tag{A.3}$$

where T_∞ is the ambient temperature (300 K).

The cooling of the quartz wall by the surrounding air is modeled using heat transfer coefficients that are, in turn, estimated from correlations [46] for natural convection from a hot plate at uniform temperature. The heat flux from the wall to the surroundings is written as

$$q_{\mathrm{cool}} = h(T_{\mathrm{w}} - T_\infty). \tag{A.4}$$

The heat transfer coefficient h is expressed in terms of the Nusselt number as

$$\mathrm{Nu} = hL/\lambda_{\mathrm{air}}, \tag{A.5}$$

where L is a reference length given by the ratio of the heat transfer surface to its perimeter. The Nusselt number is estimated using the following empirical correlations for external natural convection flows,

$$\mathrm{Nu} = \begin{cases} 0.68 + \dfrac{0.67\ \mathrm{Ra}^{1/4}}{(1 + (0.492/\mathrm{Pr})^{9/16})^{4/9}} & \text{(lateral wall)}, \\ 0.54\ \mathrm{Ra}^{1/4} & \text{(top wall)}, \\ 0.27\ \mathrm{Ra}^{1/4} & \text{(bottom wall)}. \end{cases} \tag{A.6}$$

The Rayleigh number is given by

$$\mathrm{Ra} = \frac{\rho_{\mathrm{air}}^2 g L^3 (T_{\mathrm{w}} - T_{\infty})}{\eta_{\mathrm{air}}^2 T_{\mathrm{ref}}} \mathrm{Pr}, \tag{A.7}$$

where the reference temperature is $T_{\mathrm{ref}} = (T_{\mathrm{w}} + T_{\infty})/2$, and the Prandtl number is Pr = 0.69. Furthermore, the air properties are estimated using simple power laws as a function of the temperature [10].

The heat flux due to conduction inside the quartz wall is given by

$$q_{\mathrm{cond,w}} = -\lambda_{\mathrm{w}} \nabla T \cdot n_{\mathrm{w},i}, \tag{A.8}$$

where λ_{w} is the thermal conductivity of the quartz wall (1.88×10^5 in cgs units) and $n_{\mathrm{w},i}$ is the outward normal to the wall element on its ith face. Similarly, the heat flux due to conduction from the hot gases inside the reactor may be expressed as

$$q_{\mathrm{cond,g}} = -\lambda \nabla T \cdot n_{\mathrm{w},i}, \tag{A.9}$$

where λ is the thermal conductivity of the gases inside the reactor.

ACKNOWLEDGMENTS

The authors thank Dr. K. Prasad for his assistance in preparing part of the figures and to R. Dobbins for implementing part of the surface chemistry library. This research was supported in part by the Laboratoire Central de Recherches, Thomson CSF, France.

REFERENCES

1. M. Razeghi, *The MOCVD Challenge* (Adam Hilger, Bristol/Philadelphia, 1989).
2. G. B. Stringfellow, *Organometallic Vapor-Phase Epitaxy: Theory and Practice* (Academic Press, San Diego, 1989).
3. J. Van de Ven, G. M. J. Rutten, M. J. Raaijmakers, and L. J. Giling, *J. Cryst. Growth* **76,** 352 (1986).
4. A. B. Bulsari, M. E. Orazem, and J. G. Rice, *J. Cryst. Growth* **92,** 294 (1988).
5. J. Ouazzani, K.-C. Chiu, and F. Rosenberg, *J. Cryst. Growth* **91,** 497 (1988).
6. R. J. Field, *J. Cryst. Growth* **97,** 739 (1989).
7. W. L. Holstein, J. L. Fitzjohn, E. J. Fahy, P. W. Glimour, and E. R. Schmelzer, *J. Cryst. Growth* **94,** 131 (1989).
8. E. P. Visser, C. R. Kleijn, C. A. M. Govers, C. J. Hoogendoorn, and L. J. Giling, *J. Cryst. Growth* **94,** 929 (1989).
9. D. I. Fotiadis, S. Kieda, and K. F. Jensen, *J. Cryst. Growth* **102,** 441 (1990).
10. D. I. Fotiadis, M. Boekholt, K. F. Jensen, and W. Richter, *J. Cryst. Growth* **100,** 577 (1990).
11. A. N. Jansen, M. E. Orazem, B. A. Fox, and W. A. Jesser, *J. Cryst. Growth* **112,** 316 (1991).
12. H. K. Moffat and K. F. Jensen, *J. Cryst. Growth* **77,** 108 (1986).
13. H. K. Moffat and K. F. Jensen, *J. Electrochem. Soc.* **135,** 459 (1988).
14. S. Rhee, J. Szekely, and O. J. Ilegbusi, *J. Electrochem. Soc.* **134,** 2552 (1987).
15. J. Ouazzani and F. Rosenberger, *J. Cryst. Growth* **100,** 545 (1990).
16. K. F. Jensen, D. I. Fotiadis, and T. J. Mountziaris, *J. Cryst. Growth* **107,** 1 (1991).
17. M. Tirtowidjojo and R. Pollard, *J. Cryst. Growth* **93,** 108 (1988).
18. M. Tirtowidjojo and R. Pollard, *J. Cryst. Growth* **98,** 420 (1989).
19. M. E. Coltrin and R. J. Kee, *Mat. Res. Soc. Symp. Proc.* **145,** 119 (1989).
20. M. E. Coltrin, R. J. Kee, and G. H. Evans, *J. Electrochem. Soc.* **136,** 819 (1989).
21. R. M. Zurn, Ph.D. dissertation, Yale University, Department of Mechanical Engineering, 1989 (unpublished).
22. A. Ern, Ph.D. dissertation, Yale University, Department of Mechanical Engineering, 1994 (unpublished).
23. T. J. Mountziaris and K. F. Jensen, *J. Electrochem. Soc.* **138,** 2426 (1991).
24. M. Masi, H. Simka, K. F. Jensen, T. F. Kuech, and R. Potemski, *J. Cryst. Growth* **124,** 483 (1992).
25. A. Ern and V. Giovangigli, *Multicomponent Transport Algorithms,* Lecture Notes in Physics, New Series Monographs, Vol. 24 (Springer-Verlag, Heidelberg, 1994).
26. R. J. Kee, F. M. Rupley, and J. A. Miller, Sandia Report, SAND 89–8009, 1989 (unpublished).
27. F. Sotiropoulos and S. Abdallah, *J. Comput. Phys.* **103,** 336 (1992).
28. S. W. Armfield, *Comput. Fluids* **20,** 1 (1991).
29. T. B. Gatski, *Appl. Numer. Math.* **7,** 227 (1991).
30. A. Ern and M. D. Smooke, *J. Comput. Phys.* **105,** 58 (1993).
31. G. Guevremont, W. G. Habashi, P. L. Kotiuga, and M. M. Hafez, *J. Comput. Phys.* **107,** 176 (1993).
32. A. Ern, C. C. Douglas, and M. D. Smooke, *Int. J. Supercomput. Appl.* **9,** 167 (1995).
33. L. S. Han, *Trans. ASME J. Appl. Mech.* **82,** 403 (1960).
34. A. Ern and V. Giovangigli, *J. Comput. Phys.* **120,** 105 (1995).
35. A. Ern and V. Giovangigli, *J. Chem. Vapor Depos.* **3,** 3 (1995).
36. V. Giovangigli, *Impact Comput. Sci. Eng.* **3,** 244 (1991).
37. V. Giovangigli and N. Darabiha, "Vector Computers and Complex Chemistry Combustion," in *Mathematical Modeling in Combustion and Related Topics,* edited by C. Brauner and C. Schmidt-Laine, NATO Adv. Sci. Inst. Ser. E, Vol. 140 (Nijhoff, Dordrecht, 1988), p. 491.
38. P. Deuflhard, *Numer. Math.* **22,** 289 (1974).
39. V. Giovangigli and M. D. Smooke, *Appl. Numer. Math.* **5,** 305 (1989).
40. J. O. Olsson, O. Lindgren, and O. Anderson, *Combust. Sci. Technol.* **77,** 319 (1991).
41. Y. Reuven, M. D. Smooke, and H. Rabitz, *J. Comput. Phys.* **64,** 27 (1986).
42. D. H. Reep and S. K. Ghandhi, *J. Electrochem. Soc.* **130,** 675 (1983).
43. E. O. Einset, K. F. Jensen, and C. R. Kleijn, *J. Crystal Growth* **132,** 483 (1993).
44. T. F. Kuech and E. Veuhoff, *J. Crystal Growth* **68,** 148 (1984).
45. R. Siegel and J. R. Howell, *Thermal Radiation Heat Transfer* (McGraw–Hill, New York, 1981).
46. J. P. Holman, *Heat Transfer,* 7th ed. (McGraw–Hill, New York, 1990).